

INTERNATIONAL LARGE DETECTOR

IDR

ILD Detector Collaboration

2019

ILD Editors

Main Editors:

Ties Behnke, Kiyotomo Kawagoe

Detector layout, technologies and Integration:

Karsten Buesser, Claude Vallee

Physics:

Keisuke Fujii, Jenny List

Software:

Frank Gaede, Akiya Miyamoto

Performance:

Keisuke Fujii, Jenny List

Costing:

Henri Videau, Karsten Buesser

Contents

Contents	i
1 Detector and Physics Performance	1
1.1 System performance	1
1.1.1 Tracking	1
1.1.2 Particle Flow performance and JER	1
1.1.3 Vertexing	1
1.1.4 Photon Reconstruction	1
1.1.5 Lepton ID	1
1.1.6 Charged Particle identification	1
1.2 High-level Reconstruction Performance	4
1.2.1 Flavour-Tag Performance	4
1.2.2 Hadronically decaying τ ID	4
1.2.3 Baryons / Meson reconstruction	7
1.3 Physics Benchmarks	7
1.3.1 Hadronic Branching Ratios of the Higgs Boson	7
1.3.2 Higgs Mass from $ZH \rightarrow llb\bar{b}$	8
1.3.3 Branching Ratio of $H \rightarrow \mu^+\mu^-$	11
1.3.4 Sensitivity to $H \rightarrow$ invisible	12
1.3.5 τ polarisation, in $e^+e^- \rightarrow \tau^+\tau^-$	14
1.3.6 Hadronic WW and ZZ separation in Vector Boson Scattering	15
1.3.7 Photon Energy Scale Calibration from $e^+e^- \rightarrow \gamma Z \rightarrow \gamma\mu^+\mu^-$	17
1.3.8 A_{FB} and A_{LR} from $e^+e^- \rightarrow b\bar{b}$	19
1.3.9 A_{FB} and A_{LR} from $tt \rightarrow bbqql\nu$	19
1.3.10 Discovery Reach for extra Higgs Bosons in $e^+e^- \rightarrow Zh$	22
1.3.11 Discovery Reach for and Characterisation of low ΔM Higgsinos	22
1.3.12 WIMP Discovery Reach and Characterisation in the Mono-Photon Channel	22

1 Detector and Physics Performance

The overall performance of the ILD detector is a combination of the excellent resolutions and efficiencies of the individual sub-detectors and the sophisticated reconstruction and analysis algorithms described in the previous chapter. Here we review this performance, beginning with the pure system performance that is achieved from reconstructing individual long lived particles, followed by the high-level reconstruction of jets and physics objects, ending with selected detector physics benchmarks. Where applicable this performance is presented for the large (IDR-L) and the small (IDR-S) detector model.

Frank Gaede
5 pages

1.1 System performance

1.1.1 Tracking

The resolution of the ILD detector models is evaluated from simulation and full reconstruction of single μ samples at fixed momenta and polar angles. Fig. I-1.1 shows the results for the inverse transverse momentum resolution $\sigma(1/p_T)$ and the impact parameter resolutions $\sigma(D0)$ and $\sigma(Z0)$ in $r\phi$ and z respectively.

1.1.2 Particle Flow performance and JER

1.1.3 Vertexing

1.1.4 Photon Reconstruction

1.1.5 Lepton ID

muons, electrons

1.1.6 Charged Particle identification

dE/dx , potentially ToF, shower shapes

Figure I-1.8 shows the separation power for π/K and K/p based on the dE/dx measurement in the TPC (left) and the possible improvement that could be achieved by combining it with a *time-of-flight* (TOF) measurement (right). The TOF estimator used here is computed using the first ten calorimeter hits in the Ecal that are closed to the extrapolation of the particles momentum into the calorimeter, assuming an individual time resolution of 100 ps per hit¹.

An example in the context of physics analyses can be seen in Fig. I-1.9. It compares the performance of the charged Kaon identification based on dE/dx for the large and small detector models, as obtained from the $b\bar{b}$ and $t\bar{t}$ benchmarks described in Sec. 1.3.8 and 1.3.9, respectively. For the same efficiency, the large detector reaches a 5% higher purity due to its larger TPC radius, which results in a better dE/dx resolution.

¹While this time resolution seems realistically possible, it has to be noted that so far it has not yet been demonstrated

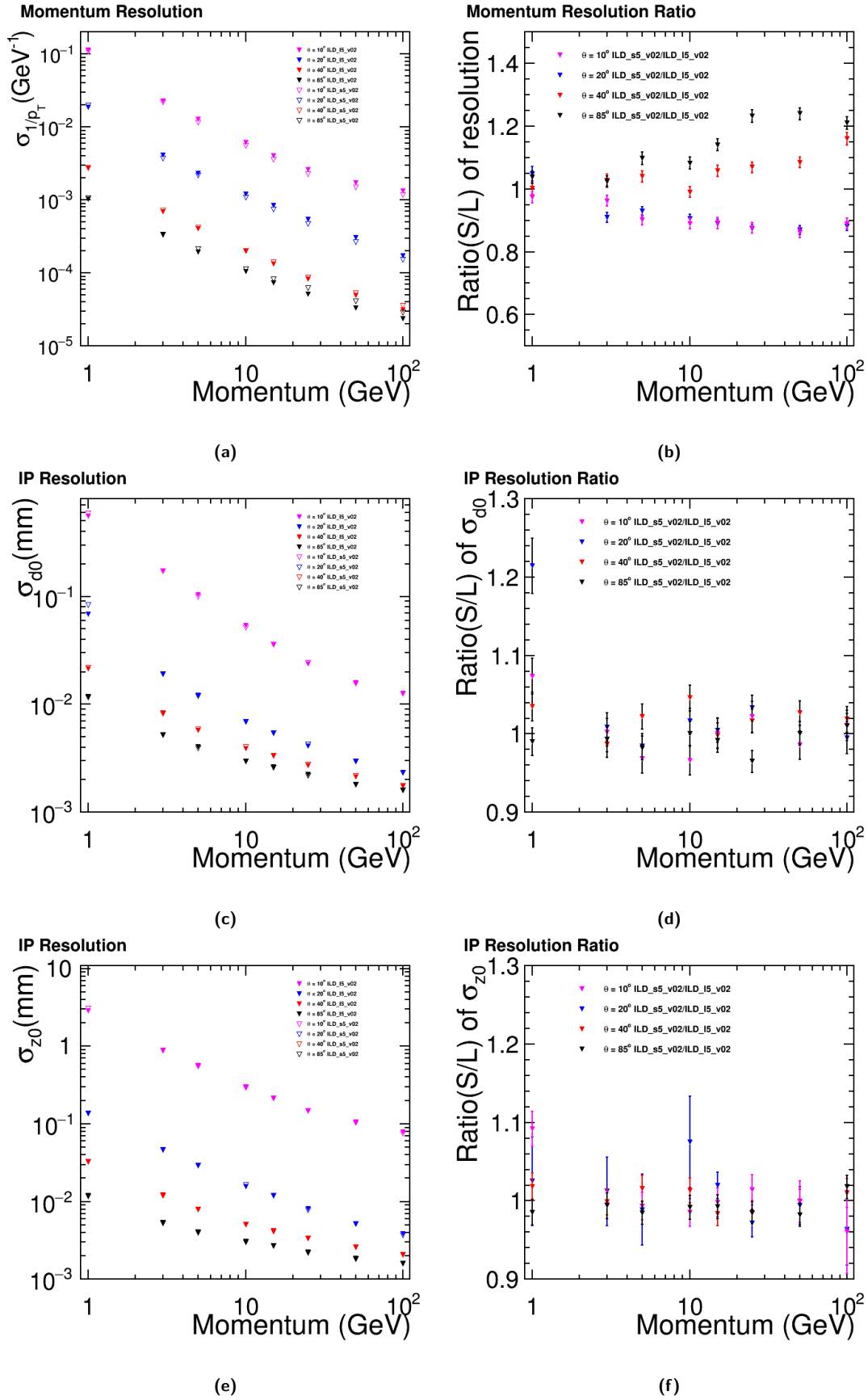


Figure I-1.1. Tracking resolutions for single muons for the large and small ILD detector models. (a) Inverse transverse momentum resolution as a function of momentum and ratio *small/large* in (b). (c) Impact parameter in $r\phi$ as a function of momentum and ratio *small/large* in (d). (e) Impact parameter in z as a function of momentum and ratio *small/large* in (f).

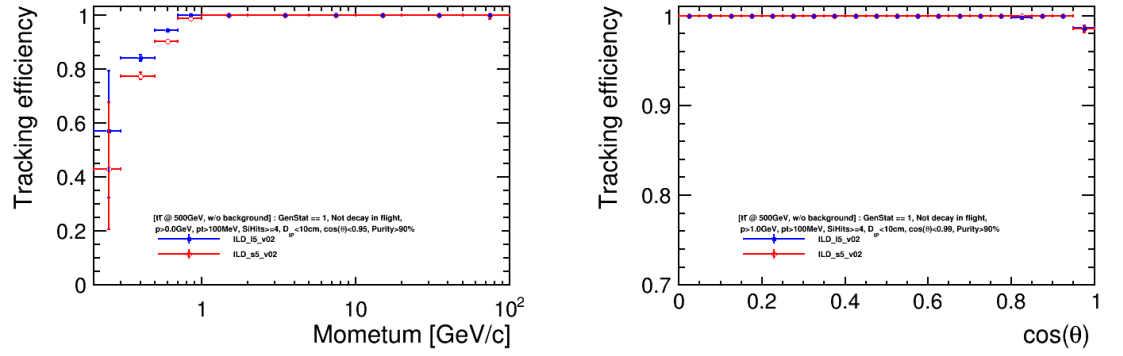


Figure I-1.2. Track finding efficiency for $t\bar{t}$ -events at 500 GeV, as a function of momentum (left) and $\cos(\theta)$ (right) for the large (red) and small (blue) ILD detector models.

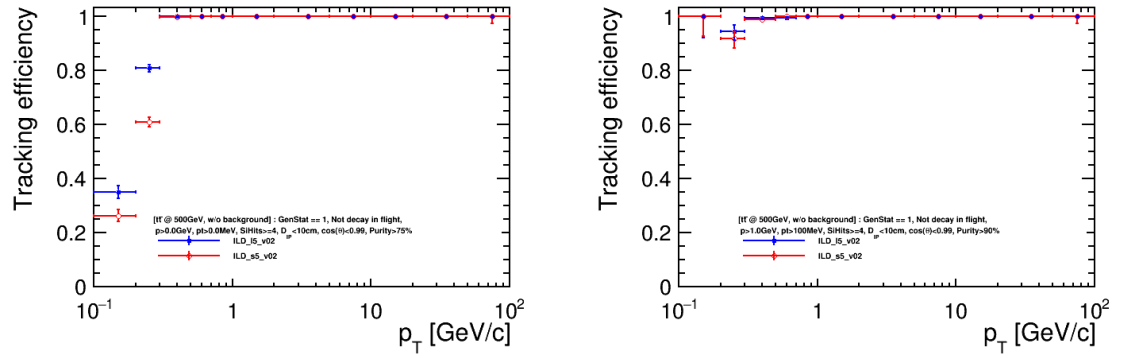


Figure I-1.3. Track finding efficiency for $t\bar{t}$ -events at 500 GeV, as a function of transverse momentum for the large (red) and small (blue) ILD detector models. left: $p > 0$ GeV ; right: $p > 1$ GeV

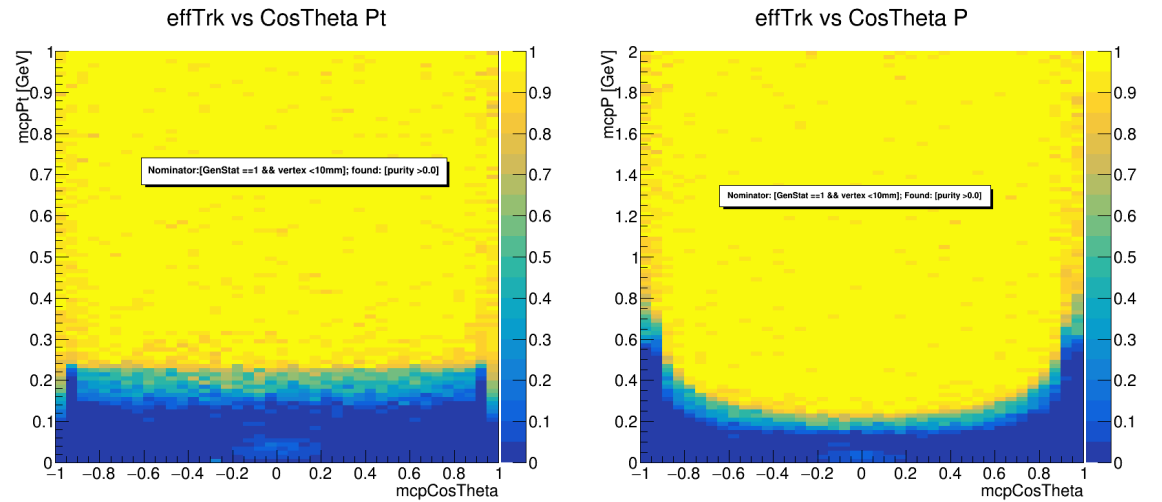


Figure I-1.4. Track finding efficiency for $t\bar{t}$ -events at 500 GeV, as a function of transverse momentum (left), momentum (right) and $\cos(\theta)$ for the large ILD detector model.

1.2 High-level Reconstruction Performance

1.2.1 Flavour-Tag Performance

1.2.2 Hadronically decaying τ ID

The correct identification of τ lepton decay modes is of particular importance in the extraction of observables sensitive to the τ lepton spin direction: examples are measurements of the τ polarisation and Higgs CP based on spin correlations in $H \rightarrow \tau\tau$ decays. Hadronic τ decays are typically offer the most sensitivity to the spin, due the presence of a single neutrino. The identification of these hadronic decay modes can be factorised into the charged and neutral components. The charged part is typically rather straight-forward in the TPC of ILD, so we concentrate efforts on understanding the

in a test beam prototype.

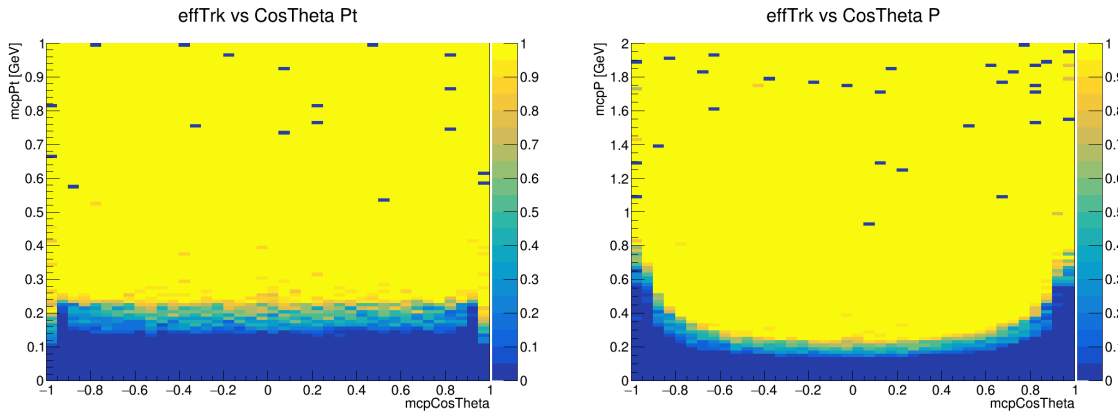


Figure I-1.5. Track finding efficiency for single muons as a function of transverse momentum (left), momentum (right) and $\cos(\theta)$ for the large ILD detector model. **FG: do we need these single particle eff. plots ?**

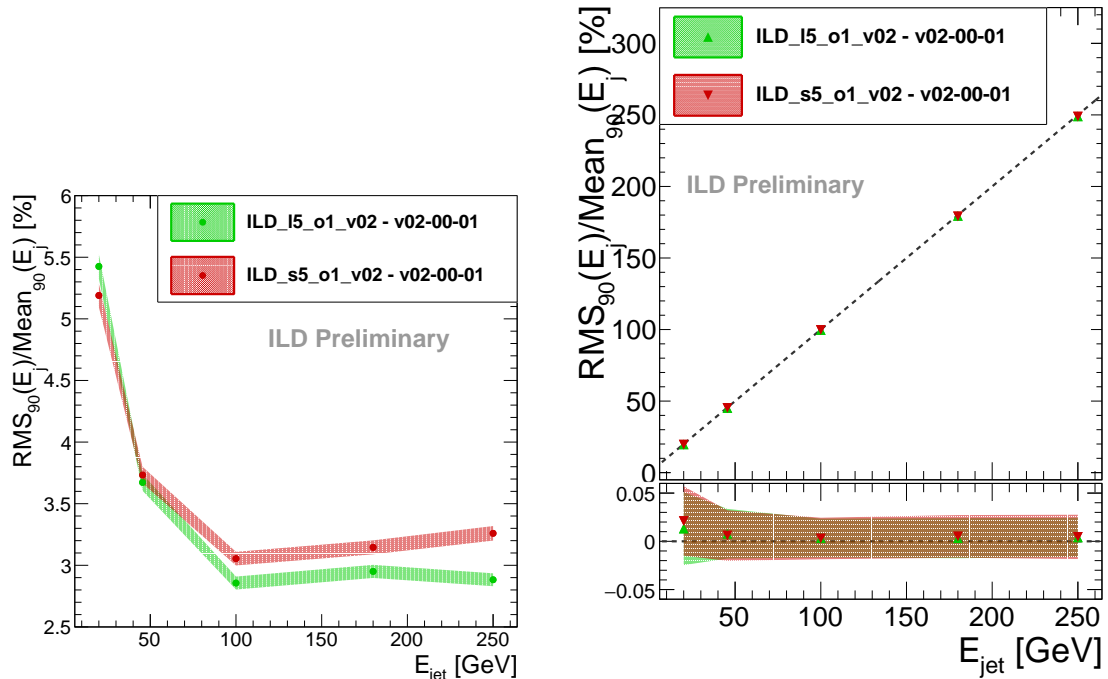


Figure I-1.6. Jet energy resolution (left) and jet energy scale (right) for the large and small ILD detector models as a function of the jet energy for uds di-jet events.

identification of the neutral part, which consists largely of photons from neutral pion (and to a lesser extent other neutral meson) decays. In the decays of highly boosted taus, these photons are typically rather close to both a charged particle and one or more additional photons produced in the same τ decay. The separation between these photons in the calorimeter depends on its inner radius, while the distance to charged particles additionally depends on the magnetic field strength. We can therefore expect some differences in performance for the large and small ILD detector models.

The performance of τ decay mode identification was studied in τ -pair production events at a centre-of-mass energy of 500 GeV. These very highly boosted τ decays are the most challenging to reconstruct due to the small distance between particles in the highly collimated τ decay jets. The standard ILD reconstruction algorithms were applied to these events.

In each event, two high momentum, back-to-back, charged PFOs were identified as τ jet "seeds".

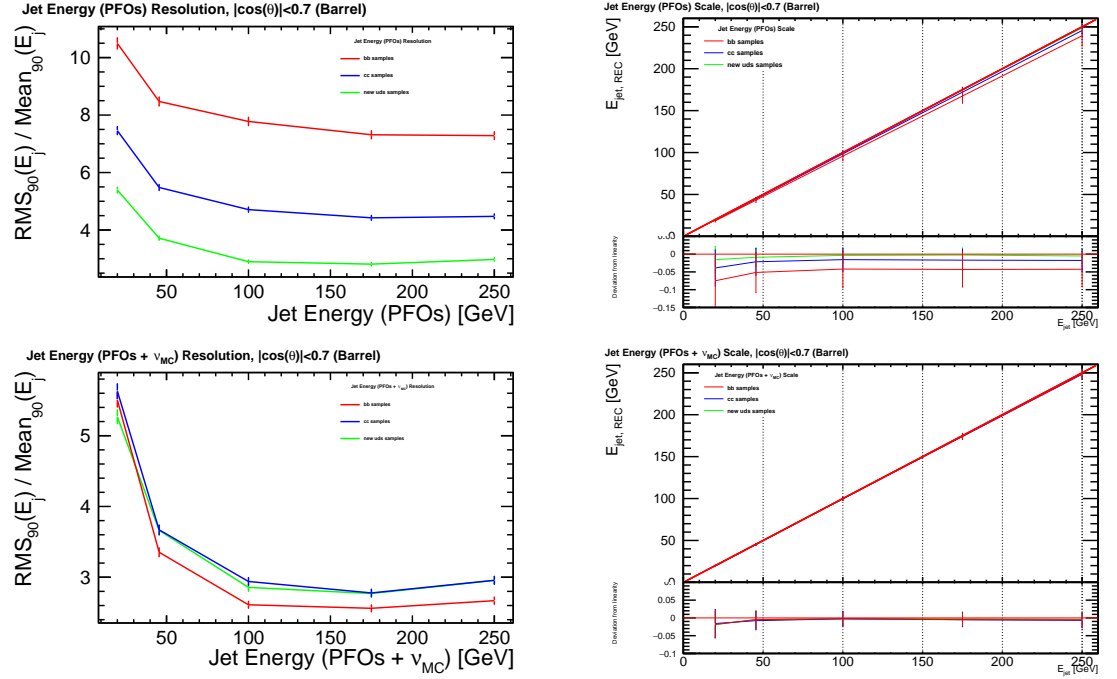


Figure I-1.7. Jet energy resolution (left) and jet energy scale (right) for uds, cc and bb events as a function of the jet energy in the large ILD detector model. Top row: without correction. Bottom row: with correcting the neutrino energy using the Monte-Carlo truth value.

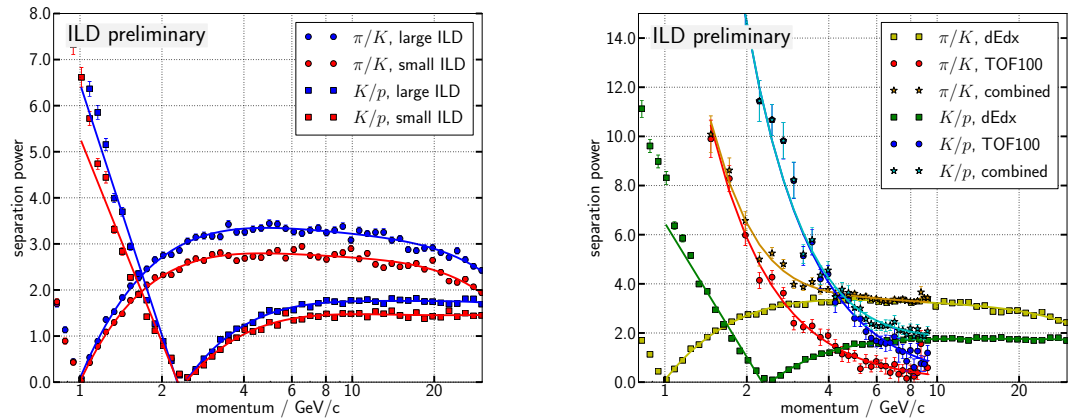


Figure I-1.8. Left: Particle separation power for π/K and K/p (left) based on the dE/dx measurement in the TPC. Right: improvement of the same separation power if combined with a *time-of-flight* (TOF) estimator from the first ten Ecal layers.

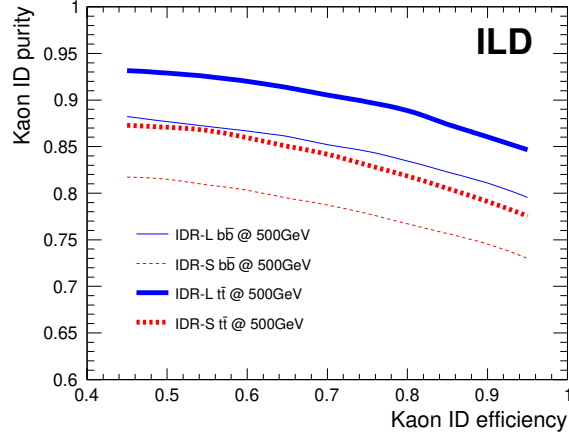


Figure I-1.9. Efficiency-purity curves for charged Kaon identification in the context of the $t\bar{t}$ and $b\bar{b}$ analyses. For the same efficiency, the large detector reaches a 5% higher purity due to its larger TPC radius, which results in a better dE/dx resolution. Details on the analyses can be found in Sec. 1.3.8 and 1.3.9.

Figure I-1.10 shows the number of photon PFOs identified in a cone around these τ seed tracks, in the case when the τ lepton decayed to $\pi^\pm\pi^0\nu$. In these events, exactly two photons are expected in the vast majority of cases. The distribution shows that it is challenging to reconstruct both photons: in around half of the cases only a single photon cluster was reconstructed, which is due to the merging of the two photons into a single reconstructed particle. A difference is seen between the two detector models, with the large version somewhat more often correctly resolving the two photons, which can be understood as being due to the larger ECAL radius increasing the distance between the photons' electromagnetic showers.

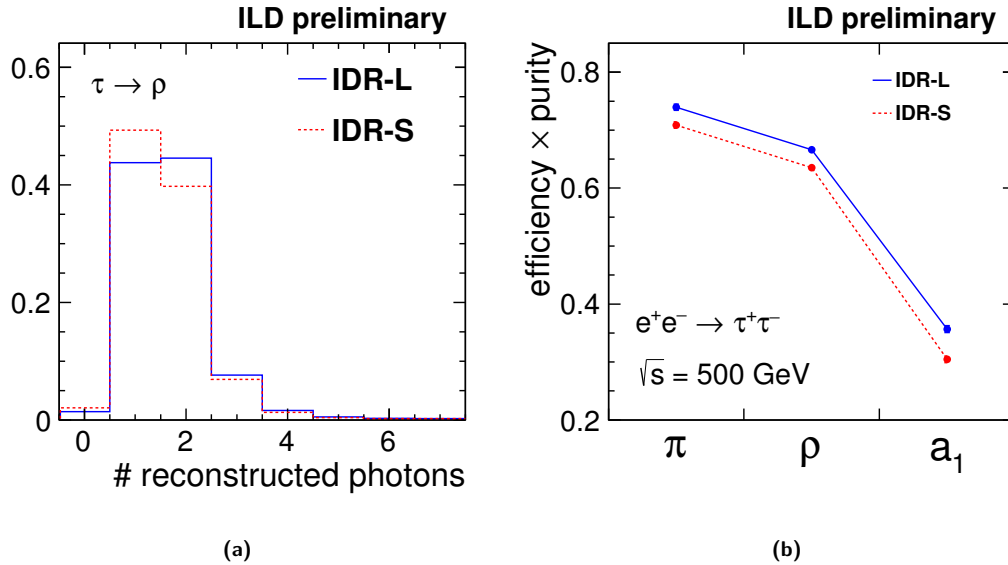


Figure I-1.10. Hadronic decay mode identification for isolated τ -leptons with momenta near 250 GeV. (a) The number of reconstructed photon PFOs in $\tau \rightarrow \rho\nu \rightarrow \pi^\pm\pi^0\nu$. (b) The performance of a simple τ decay mode identification algorithm.

A simple cut-based approach to the identification of single-prong hadronic τ decays was developed, based on the number of reconstructed photon PFOs, and the invariant mass of this set of photon PFOs both alone and together with the charged PFO around which the τ candidate jet was built. The ability of this algorithm to distinguish $\tau \rightarrow \pi^\pm\nu$ (" π "), $\tau \rightarrow \pi^\pm\pi^0\nu$ (" ρ "), and $\tau \rightarrow \pi^\pm\pi^0\pi^0\nu$ (" a_1 ") decays is shown in Fig. I-1.10. The product of selection efficiency and purity varies between

around 30% and 75% among these three decay modes. The large detector model performs slightly better, as expected thanks to the larger inner ECAL radius.

1.2.3 Baryons / Meson reconstruction

- $\Lambda_c^+ \rightarrow pK^-\pi^+$
- D^0, D^*
- $J\Psi \rightarrow \mu\mu$ / inclusive di-muon spectrum ?

Keisuke Fujii, Jenny List
10 pages

1.3 Physics Benchmarks

The performance of the two ILD detector models IDR-L and IDR-S has been evaluated on a number physics benchmarks, which will be discussed in this section. Despite the fact that a 250-GeV version of the ILC is currently under political consideration in Japan, the detector benchmarking has been performed at higher center-of-mass energies, mostly at 500 GeV, and in one case even at 1 TeV. This choice has been made in order to make sure that both detector models perform adequately also under the more challenging experimental conditions of the higher energy stages, and in order to cover e.g. a wider range of jet, lepton and photon energies.

Unless stated otherwise, all results have been scaled to the integrated luminosity and beam polarisation of the full H20 running scenario originally defined in [1], which is — for the higher center-of-mass energies — unchanged since [2]. In particular, the H20 scenario comprises 4 ab^{-1} at 500 GeV, with beam polarisation absolute values of 80% for the electron and 30% for the positron beam. The total luminosity is shared between the different polarisation sign combinations according to $f(-+, +-, ++, --) = (40\%, 40\%, 10\%, 10\%)$. Analogously, 8 ab^{-1} are considered at 1 TeV, with absolute polarisation values of 80% for the electron and 30% for the positron beam, with the same $f(-+, +-, ++, --) = (40\%, 40\%, 10\%, 10\%)$ sharing.

The benchmarks presented in this section have been carefully chosen to illustrate many performance aspects with a minimum number of benchmarks, and are not to meant to cover *complete* physics case. The main focus of the analysis work was not always the pure optimisation for utmost physics performance, but rather to better understand and highlight the role of individual performance aspects and their interplay.

Unless stated otherwise, the analyses performed for and since the time of the ILC TDR remain valid in their physics message. For an up-to-date review of the ILC physics case, based on ILD detector simulation, see e.g. [2].

1.3.1 Hadronic Branching Ratios of the Higgs Boson

The measurement of the hadronic branching ratios of the Higgs boson, including in particular $H \rightarrow c\bar{c}$, is one of the unique items on the menu of future e^+e^- colliders. This crucially depends on an excellent flavour tag, c.f. Sec. 1.2.1, enabled by vertex detectors with micrometer point resolution with a first layer placed as close as 1.4 cm to the beam line.

As a benchmark, the $\nu\bar{\nu}H \rightarrow \nu\bar{\nu}jj$ final state was chosen in order to minimize the impact of other performance aspects like e.g. jet clustering. Thus the target physics observable here is $\sigma(\nu\bar{\nu}H) \times BR(H \rightarrow b\bar{b}/c\bar{c}/gg)$. With the full 500 GeV data set, about 200000 $H \rightarrow b\bar{b}$ events would be produced in this final state alone, while about 30000 and 10000 $H \rightarrow gg$ and $H \rightarrow c\bar{c}$ would be available, respectively. In the limit of 100% signal efficiency and zero background, this

would correspond to statistical precisions of 0.2%, 0.6% and 1% for $H \rightarrow b\bar{b}$, $H \rightarrow gg$ and $H \rightarrow c\bar{c}$, respectively.

The benchmark analysis is documented in detail in [3], and follows earlier analyses [4–6]. The full performance of the ILC on Higgs branching ratio measurements, combining all final states, can be found in [2]. After a cut-based preselection, the kinematic selection of $\nu\bar{\nu}H \rightarrow \nu\bar{\nu}jj$ events is refined by a multi-variate approach. Up to this point, no flavour-tag information is used.

[JL: reconstructed M_H for large and small, signal and backgrounds ?]

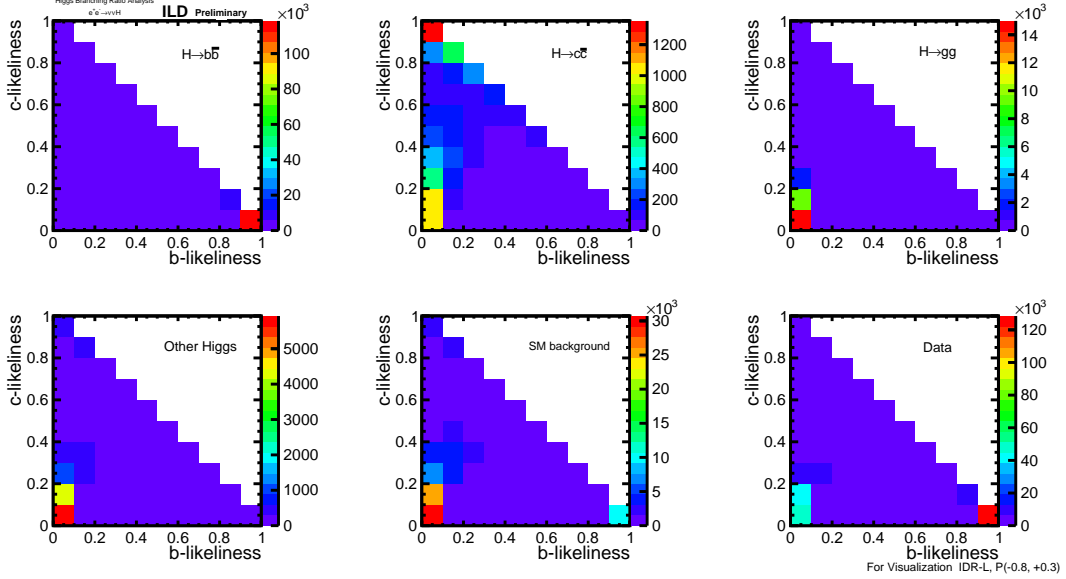


Figure I-1.11. Visualisation of the flavour tag performance in $\nu\bar{\nu}H$. The panels show the 2D distributions of c - vs b -likeliness separately for $H \rightarrow b\bar{b}$, $H \rightarrow c\bar{c}$, $H \rightarrow gg$, $H \rightarrow \text{other}$, the SM background and their mix expected in data.

Figure I-1.11 shows the 2D distributions of c - vs b -likeliness (c.f. Sec. 1.2.1) for the different Higgs decay modes. The “data” distribution is then fitted in 3D template approach² in order to determine the contained fractions of the various hadronic Higgs decay modes. The resulting precisions from this template fit are displayed in Fig. I-1.12. Thereby, Fig. I-1.12a compares the actual results for IDR-L and IDR-S with the $P(e^-, e^+) = (-80\%, +30\%)$ data only with the result obtained for a perfect flavour tag. It shows that for $H \rightarrow b\bar{b}$ and $H \rightarrow gg$ the current flavour tag performance yields a close to perfect identification of these final states. For $H \rightarrow c\bar{c}$, however, the real flavour tag performs worse by a factor of two. On the otherhand, for a worse flavour separation, especially the expected precision for $H \rightarrow c\bar{c}$ degrades rapidly [3], thus the performance of the ILD detector and reconstruction is crucial for the ability to measure $H \rightarrow c\bar{c}$.

Figure I-1.12b finally compares the precisions from all data sets combined for IDR-L and IDR-S. It shows a rather equivalent performance of both detector models. In the case of $H \rightarrow c\bar{c}$, which is most sensitive to the detector performance, the smaller detector model actually performs a little better due to its stronger magnetic field and the resulting better momentum resolution in the forward region, c.f. Fig. I-1.1.

1.3.2 Higgs Mass from $ZH \rightarrow l\bar{l}b\bar{b}$

The single most precise method to measure the Higgs mass is the recoil analysis at $\sqrt{s} = 250$ GeV [7]. At \sqrt{s} much higher than the ZH production threshold, the recoil technique suffers substantially

²including also the bc -likeliness, and a much smaller number of bins [3]

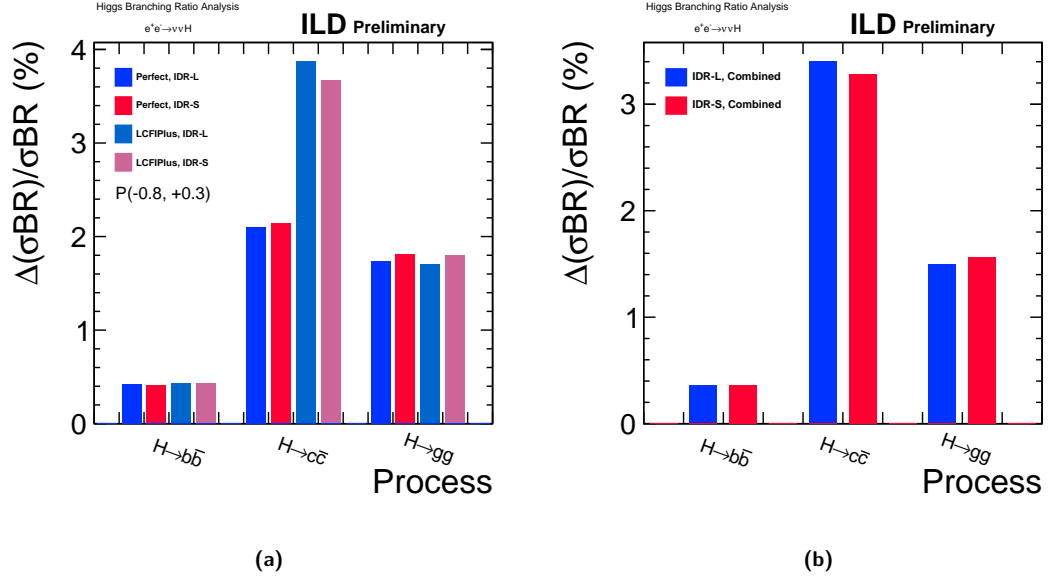


Figure I-1.12. (a) Comparison of current and ideal flavour tag performance. The precision on $H \rightarrow c\bar{c}$ is most sensitive to the actual flavour tag performance. (b) Comparison of IDR-L and IDR-S for all polarisation configurations combined.

from the increasing amount of ISR and beamstrahlung. In addition, the momenta of the muons from $Z \rightarrow \mu\mu$ increase in magnitude and thus are measured less precisely. Still, the data collected at higher centre-of-mass energies can be exploited effectively when using the fully-reconstructable decay modes of the Higgs boson in combination with kinematic constraints from the known initial state. E.g. the constraints $\sum_i p_{iy} = 0$ and $\sum_i p_{ix} = 3.5 \text{ GeV}^3$ can replace the measured energies of the Higgs decay products, so that only on the *angles* of the Higgs decay products and the momenta of the muons from $Z \rightarrow \mu^+\mu^-$ enter in the mass reconstruction. Thus the technique is independent of systemic uncertainties as e.g. associated with the b -jet energy scale. The detailed description of the technique can be found in [8].

The resolutions on the kinematic quantities which enter the Higgs mass reconstruction, namely azimuthal and polar angles of the jets and the muon energy, are compared in Figs. I-1.13a and I-1.14 for IDR-L and IDR-S. Thereby, the jet angles obtained from clustering the MC particles after hadronisation serve as truth reference, so that the detector performance is singled out from other influences. Figure I-1.13b illustrates the effect of hadronisation by comparing to the quark-level direction taking IDR-L as example. It shows that the detector resolution (blue histogram, same as in Fig. I-1.13a) is comparable, but subdominant to the hadronisation effect (red histogram). While the angular resolutions are very similar for both detector models, the muon energy resolution is worse for the small detector, reflecting the somewhat worse p_t resolution for high-momentum tracks in the central region of the detector, c.f. Fig. I-1.1.

Figure I-1.15 shows the propagation of this effect to the actual physics observable, i.e. the reconstructed mass of the Higgs candidates. IDR-L and IDR-S are compared for the muon channel in Fig. I-1.15a and for the electron channel in Fig. I-1.15b. In both cases signal and all backgrounds from the SM and other ZH modes are combined, with clear peaks visible around the nominal Higgs and Z boson masses. In particular in the muon channel, the worse momentum resolution of the small detector leads to the peaks being visibly wider. This results in an increase of the uncertainty on the measured Higgs mass by about 22%, from 66 MeV in the case of IDR-L to 81 MeV for IDR-S. [JL: How are these numbers extracted?]

³In x direction the initial momentum is not zero due to the crossing angle of the beams, but given by $\sqrt{s} \cdot \sin 14 \text{ mrad}$.

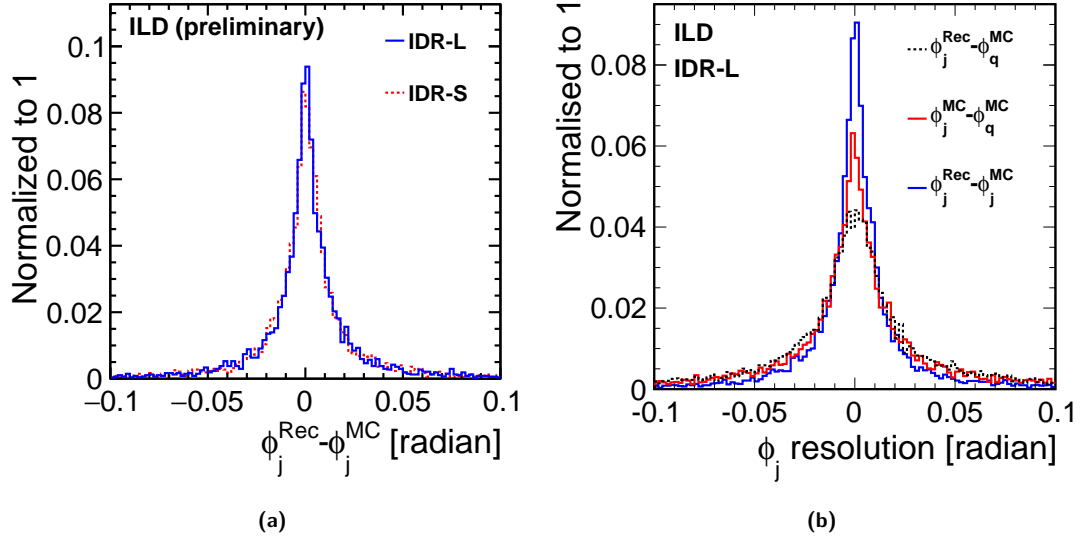


Figure I-1.13. (a) Resolution obtained with IDR-L and IDR-S for the jet azimuthal angle (b) Influence of hadronisation on the jet azimuthal angle

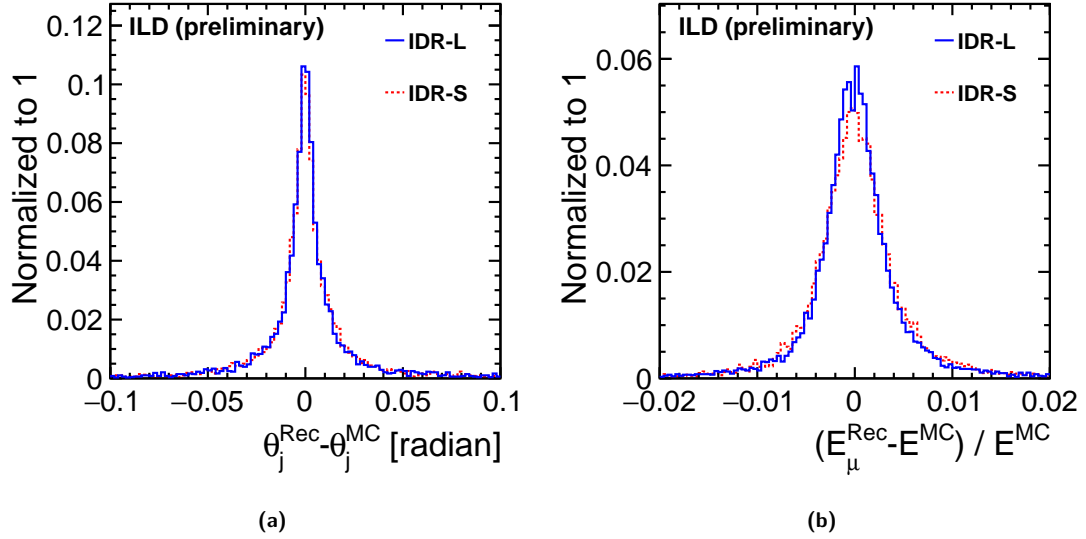


Figure I-1.14. Resolutions obtained with IDR-L and IDR-S for (a) the jet polar angle (b) the muon energy, after recovery of FSR photons.

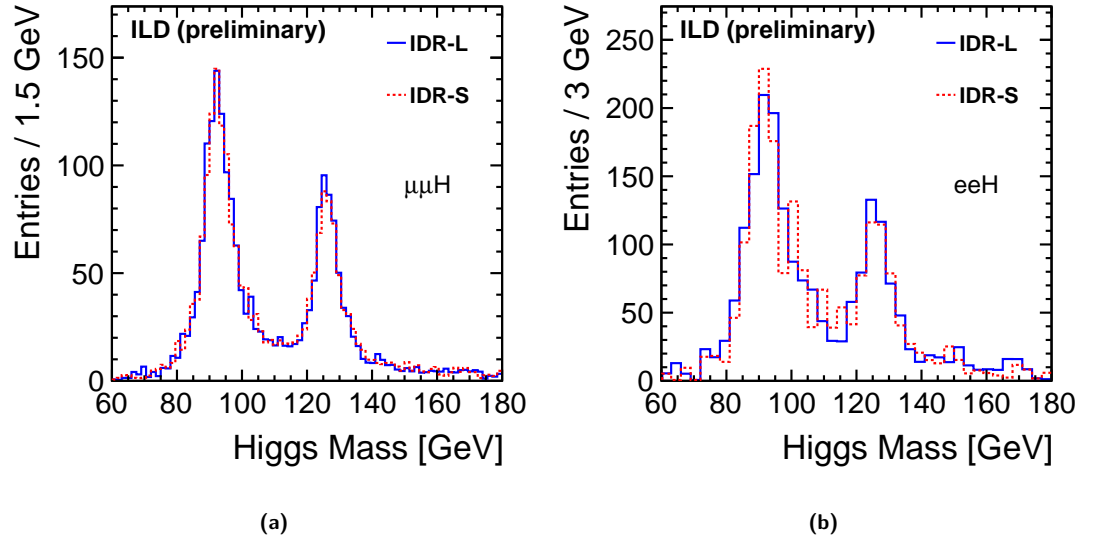


Figure I-1.15. reconstructed Higgs mass distribution for signal and background for IDR-L and IDR-S (a) muon channel (b) electron channel (here with limited MC statistics)

1.3.3 Branching Ratio of $H \rightarrow \mu^+ \mu^-$

In the SM, the decay of the Higgs boson into a pair of muons is a very rare decay, with a branching ratio of 2.2×10^{-4} . In order to identify this small signal, the achievable mass resolution, thus the precision to which the momenta of the two muons are measured, plays a crucial role. For the purpose of detector benchmarking, we consider only $\sigma(\nu\bar{\nu}H) \times BR(H \rightarrow \mu^+ \mu^-)$ as observable, which isolates best the effect of the muon momentum resolution.

The selection [9] targets events with substantial missing four-momentum plus two well-reconstructed, oppositely charged muons. Kinematic and angular variables are exploited in an MVA analysis. Figure I-1.16a shows the di-muon invariant mass distribution for all selected signal events. In case of the small the detector model, the mass peak is about 10% wider than for the large detector. This originates from the combination of the muons from the Higgs decay being high-energetic and rather central, plus the better momentum resolution of the large detector for high-momentum tracks in the barrel. This effect is seen more clearly in Fig. I-1.16b, which compares the event-by-event resolution of the di-muon invariant mass for the selected signal events with both muons in the barrel region of the detector ($|\cos \theta| < 0.7$).

For the 500 GeV data set of the H20 scenario, the asymptotic precision on cross section times branching ratio for the case of 100% efficiency and no backgrounds would be 13%.

After the event selection, about 33 signal events, corresponding to a selection efficiency of 58%, remain over a evenly distributed background of about 1100 events (counted in a mass window between 120 and 130 GeV). Finally, the expectation values for the number of signal events observable above the backgrounds as well as for its uncertainty are obtained from many toy MC fits to the di-muon invariant mass spectrum [9]. The obtained precisions on $\sigma(\nu\bar{\nu}H) \times BR(H \rightarrow \mu^+ \mu^-)$ are 40.2% for IDR-L and 41.3% for IDR-S. The relative difference of 2.8 is consistent with the expectation of a $\sim 10\%$ difference in the signal peak width over a flat background. Either number, however, is about a factor 3 worse than the asymptotic precision for the case of 100% efficiency and no backgrounds, which would be 13%. The difference is mostly dominated by the remaining “irreducible” backgrounds with two muons and two neutrinos from W pairs decaying either directly to muons or via tau-leptons. While there is certainly room for improvement in rejecting these backgrounds, this will factorize from the impact of the signal peak width, as long as the background remains flat in the discriminating

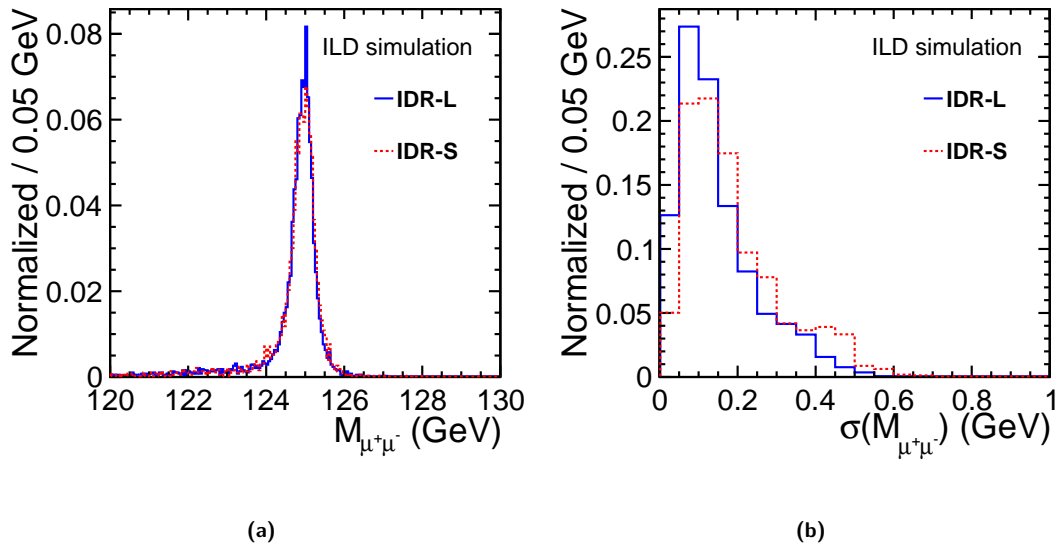


Figure I-1.16. $H \rightarrow \mu^+\mu^-$ benchmark: (a) di-muon invariant mass for all selected signal events (b) mass resolution for the case that both muons are in the barrel region of the detector ($|\cos \theta| < 0.7$)

variable.

1.3.4 Sensitivity to $H \rightarrow$ invisible

The decay of the Higgs boson into invisible particles is of particular interest because it could give important clues about the nature of Dark Matter. As a detector benchmark for testing the impact of the jet energy resolution, in particular the hadronic decay mode of the Z boson is considered here. Thus the physics observable will be the upper limit on $\sigma(q\bar{q}H) \times BR(H \rightarrow \text{inv.})$.

The event selection [10] targets events which are consistent with a di-jet plus missing four-momentum topology, where the di-jet invariant mass should be compatible with the Z boson mass. The jet finding step also serves to reject PFOs from overlay of $\gamma\gamma \rightarrow \text{low-}p_t$ hadron events. The final discriminating variable is the invariant mass of the “invisible” four-momentum recoiling against the Z boson.

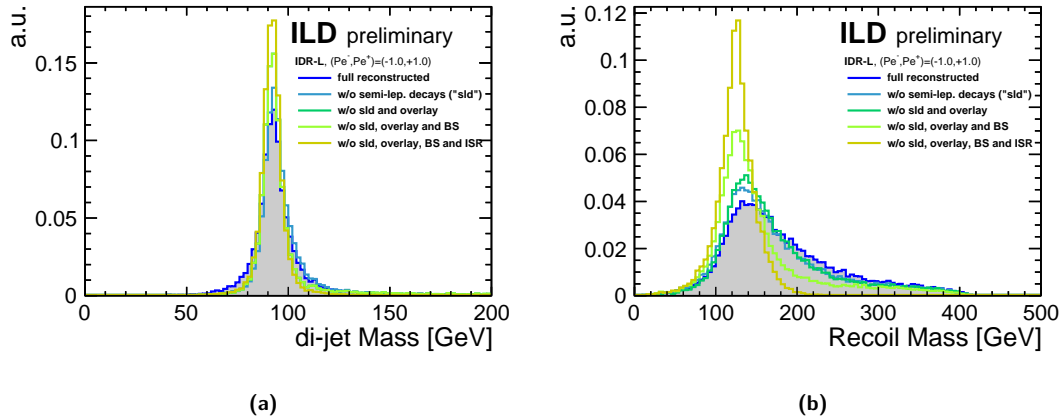


Figure I-1.17. Impact of various effects on (a) the invariant di-jet mass and (b) the recoil mass, shown for the example of the large detector model.

Figure I-1.17a shows the di-jet invariant mass for the selected signal events at various levels of realism from the full reconstruction to cheating everything but the detector and particle flow reconstruction. The first step of partial cheating removes jets with semileptonic heavy flavour decays.

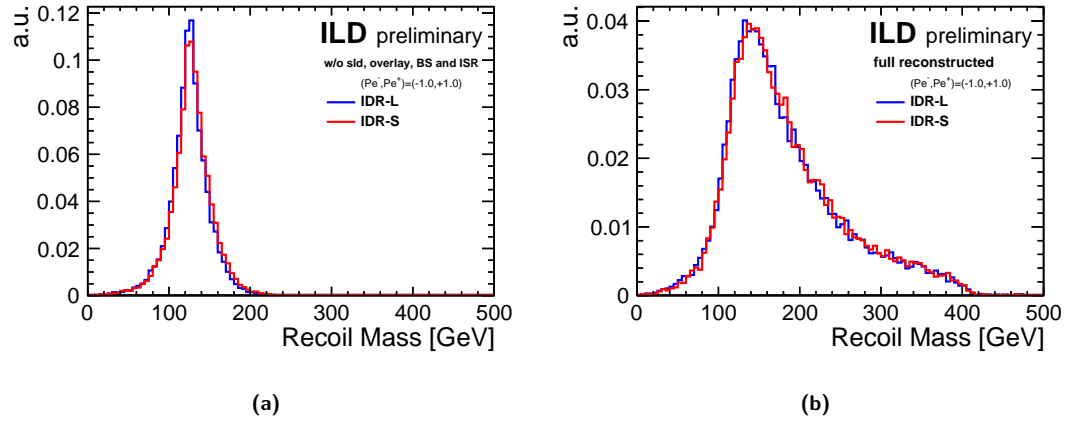


Figure I-1.18. Comparison of the recoil mass distributions for IDR-L and IDR-S (a) when cheating semi-leptonic decays, overlay removal, beam spectrum and ISR (b) at full reconstruction level.

In a detector like ILD shower shapes in the highly-granular calorimeter and specific energy loss information from the TPC should allow an excellent identification of leptons in jets, which, combined with secondary vertex information should allow to significantly improve scale and resolution for heavy flavour jets with semileptonic decays. However, the corresponding reconstruction algorithms are still under development and thus could not be applied here. Similarly, work is ongoing to improve the removal of overlay backgrounds, see e.g. Sec. 1.3.11 and Ref. [11]. Thus, we expect that with future reconstruction improvements, a performance similar to the case “w/o sld and overlay” could be reached. The beam spectrum (BS) by construction does not affect the invariant di-jet mass. ISR, on the contrary, can lead to photons in the detector. In this analysis, no attempt has been made to identify the corresponding particle flow objects. Therefore, also a large part of the effect of ISR on the di-jet mass should be recoverable with a more sophisticated analysis.

The corresponding situation for the recoil mass is shown in Fig. I-1.17b. Here, ISR and BS have a large impact since they lead to a deviation of the actual initial state of the hard interaction from the naive assumption. Again, no attempt has been made to correct the kinematics of those events in which a photon is detected, c.f. Sec 1.3.10 for an example where such a correction is applied.

The recoil mass distributions obtained with the large and small detector model are compared in Fig. I-1.18. Thereby, Fig. I-1.18b shows the situation at the current full reconstruction level, while Fig. I-1.18a cheats the effect of semi-leptonic decays, overlay removal, beam spectrum and ISR. In both cases, the recoil mass is slightly shifted to higher values in case of the small detector, due to differences in the calibration of the particle flow for the two models. In addition, the cheated recoil mass distribution is a bit wider for the small detector, as expected from its slightly worse JER, c.f. Fig. I-1.6.

The results in terms of the physics observable, namely the 95% C.L. upper limit on $\sigma(q\bar{q}H) \times BR(H \rightarrow \text{inv.})$, are summarized in Fig. I-1.19 for both detector models at the various cheating levels. In the case of full reconstruction, the upper limit is at 0.78% for IDR-L and at 0.79% for IDR-S, corresponding to a relative change of about 1%. At when isolating the effect of the particle flow performance by cheating all other aspects, the limit would be 0.50% (0.51%) for IDR-L (IDR-S), i.e. a relative change of about 2%. Also displayed is an estimate of how the cheated results would change when scaling the JER up and down. This clearly shows that larger variations of the JER, by 20% or so, have a clear impact on this physics analysis. In the case of $\sqrt{s} = 250$ GeV, the impact of ISR and BS is much smaller, increasing the relative contribution from the JER.

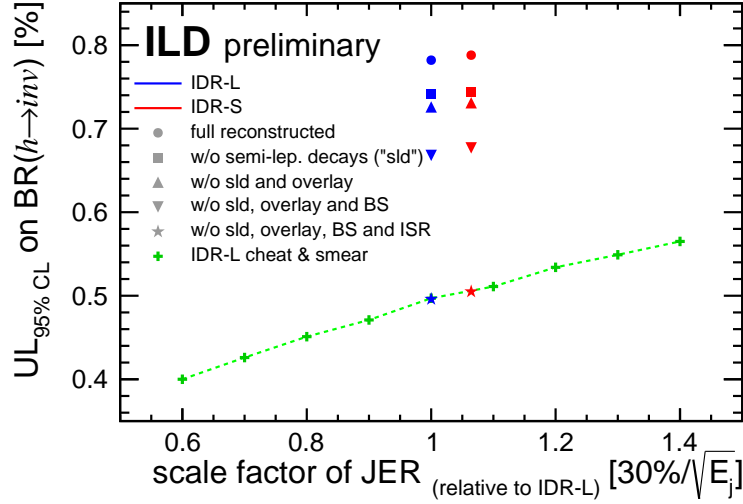


Figure I-1.19. Upper limit on $BR(h \rightarrow \text{invisible})$ at 95% C.L. as a function of the jet energy resolution. The blue and red symbols show the results obtained from simulation of the IDR-L and IDR-S detector models, respectively, in full reconstruction and at various levels of cheating. The green crosses are obtained by varying the JER up and down w.r.t. IDR-L. [JL: fix axis titles!]

1.3.5 τ polarisation, in $e^+e^- \rightarrow \tau^+\tau^-$

As shown in Sec. 1.2.2, the smaller ECAL inner radius of the small detector model slightly reduces the ability to identify the correct number of photons in highly-boosted τ decays. Using the product of efficiency times purity as a figure of merit, this leads to a 5% worse identification of $\tau \rightarrow \pi\nu$ and $\tau \rightarrow \rho\nu$ decays, while the identification of $\tau \rightarrow a_1\nu$ decays deteriorates by about 15% relative, c.f. Fig. I-1.10.

In order to evaluate the impact of this difference in a physics example, the measurement of the τ polarisation in $e^+e^- \rightarrow \tau^+\tau^-$ has been studied, looking specifically at events with no significant ISR, so those *not* returnin to the Z pole. For the $\tau \rightarrow \pi\nu$ channels, the magnitude of the π^\pm momentum can directly be used to extract the polarisation. In case of the $\tau \rightarrow \rho\nu$ decay, a polarimeter vector is constructed from the momenta of the π^\pm and the π^0 . A detailed description of the analysis and the polarisation extraction can be found in [12].

Figure I-1.20 illustrates the precision on the τ polarisation achieved with IDR-L and IDR-S based on the π and ρ channels in the $P(e^-, e^+) = (-80\%, +30\%)$ data set, which dominates the combined precision. Thereby, various levels of cheating are shown, starting from the optimal result when using all MC information, including the neutrino momentum. The next entry shows by how much the performance in the ρ channel degrades by the approximate definition of the polarimeters used here⁴. The most significant effect occurs when reducing the number of signal events according to the selection efficiency of about 55% observed in the full analysis [JL: clarify with Daniel]. The last three steps use the fully simulated and reconstructed events, apart from the entry “cheat ECAL”, which uses MC information for the π^0 in the ρ channel. In the last step, the full SM background is added. Overall, the differences between IDR-L and IDR-S are very small, and probably due to limited MC statistics. The largest deterioration of the precision occurs when applying the selection efficiency. Thus, future improvements of the di- τ selection have the largest potential for improving this measurement.

⁴In principle, improved methods can be used, which however need further investigation [12].

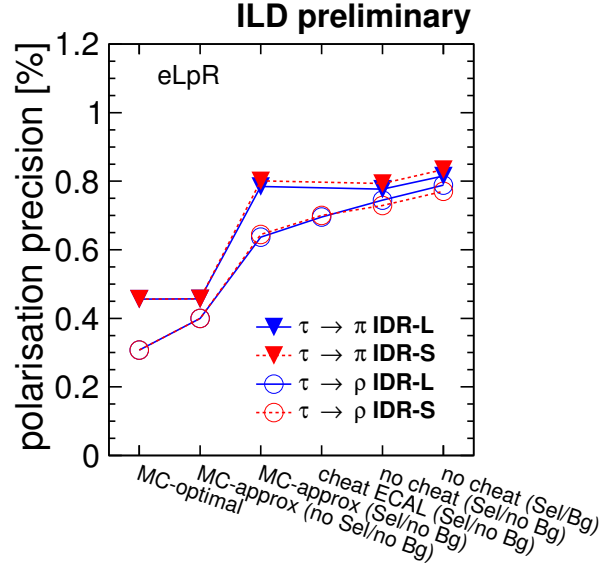


Figure I-1.20. Precision on the τ polarisation achieved with IDR-L and IDR-S at various levels of cheating (see text) based on the π and ρ channels in the $P(e^-, e^+) = (-80\%, +30\%)$ data set.

1.3.6 Hadronic WW and ZZ separation in Vector Boson Scattering

Vector boson scattering is an important process for testing the unitarisation of WW scattering by the Higgs boson, as well as for measuring quartic gauge couplings, and thereby probing for anomalous contributions. Amongst all relevant final states, the reaction $e^+e^- \rightarrow \nu\nu VV \rightarrow \nu\nu qq\bar{q}\bar{q}$, where VV can be WW or ZZ , poses a particular challenge to the detectors and reconstruction algorithms, since it requires the separation of the hadronic W and Z decays without the ability to exploit kinematic constraints e.g. on the total event energy due to the two invisible neutrinos.

This benchmark, at a center-of-mass energy of 1 TeV, has already been studied in full detector simulation for the ILD Lol [13]. Now, we include for the first time all relevant aspects, in particular the full overlay from $\gamma\gamma \rightarrow \text{low-}p_t$ hadrons and from e^+e^- pair background, and we consider all quark flavours in the final state [14]. The W and Z mass distributions obtained with the current full reconstruction are shown in Fig. I-1.21. Thereby Fig. I-1.21a shows the average di-jet mass per event, comparing ILD-L and ILD-S, while Fig. I-1.21b shows the 2-dimensional distribution in the mass plane of the two invariant di-jet masses for ILD-L. At this level, no significant difference between the detector models can be observed.

Figure I-1.22 shows the analogous distributions obtained when cheating the jet clustering (incl. the overlay removal), the jet pairing and when excluding events with semi-leptonic decays of heavy quarks, so that only the effects of the natural widths of the bosons, of fragmentation and hadronisation as well as the JER itself remain. Also here, no striking difference between the models can be seen, which leads to the conclusion that on this event sample, which is dominated by events with rather low invariant masses of the di-boson system, the effect of the slightly worse JER of ILD-S is hidden beneath the width and fragmentation/hadronisation corrections.

Nevertheless, the differences between Fig. I-1.21 and Fig. I-1.22 are striking. Therefore, we investigated the impact of the various nuisance effects individually as shown in Fig. I-1.23, for ILD-L only. For both WW and ZZ , the dominant effect is the residual of the non-perfect overlay removal, followed by the jet clustering itself and the semi-leptonic decays. Non-perfect jet pairing only plays a minor role. This result demonstrates the need for development of more sophisticated high-level reconstruction algorithms, in particular for the overlay removal, the jet clustering and the identification and correction of semi-leptonic heavy flavour decays. For all these cases promising tools are under

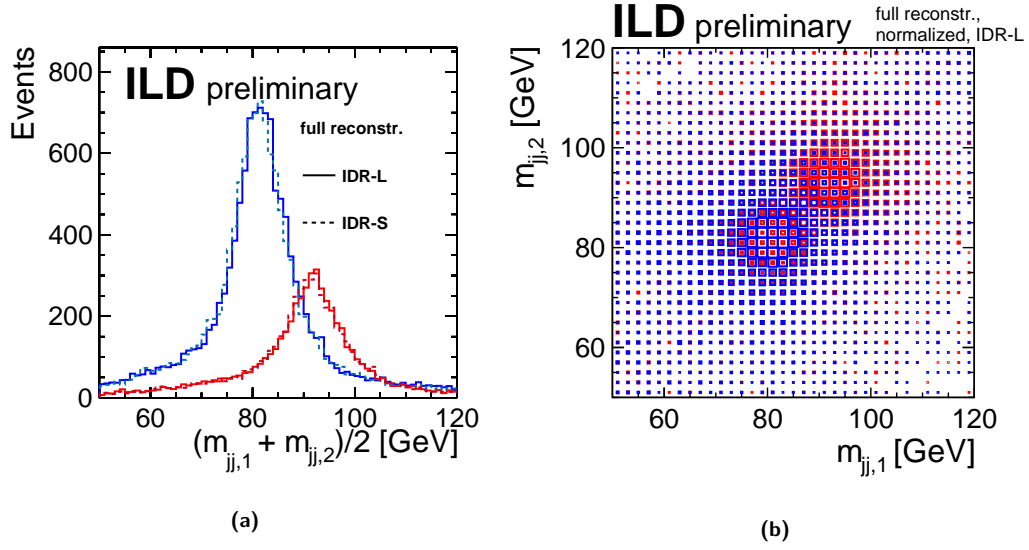


Figure I-1.21. Dijet masses in $e^+e^- \rightarrow \nu\nu WW$ and $e^+e^- \rightarrow \nu\nu ZZ$ events as obtained from the current full reconstruction.

(a) Average of the two di-jet masses per event. (b) 2D illustration of the two di-jet masses per event.

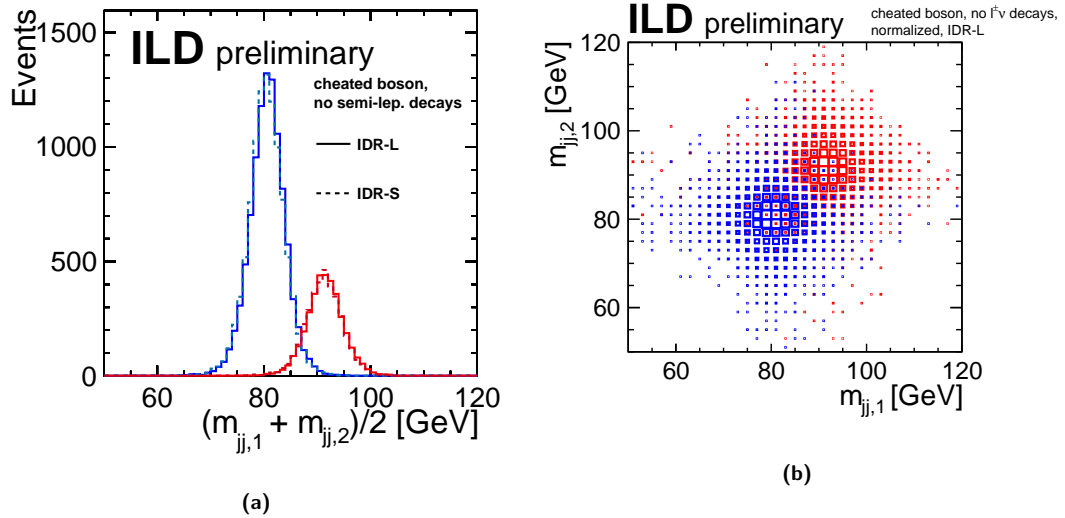


Figure I-1.22. Dijet masses in $e^+e^- \rightarrow \nu\nu WW$ and $e^+e^- \rightarrow \nu\nu ZZ$ events as obtained when cheating the jet clustering and excluding events where one (or more) jets contain semi-leptonic charm or beauty decays.

(a) Average of the two di-jet masses per event. (b) 2D illustration of the two di-jet masses per event.

development, see e.g. Sec. 1.3.11 and Ref. [11].

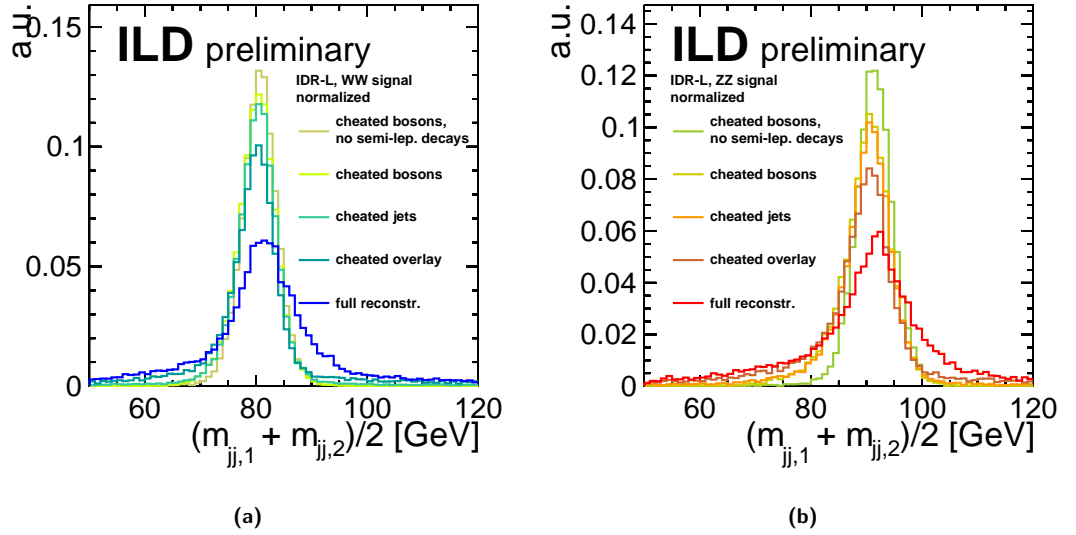


Figure I-1.23. Average di-jet masses as obtained in full reconstruction at various levels of cheating. (a) $e^+e^- \rightarrow \nu\nu WW$ events. (b) $e^+e^- \rightarrow \nu\nu ZZ$ events.

1.3.7 Photon Energy Scale Calibration from $e^+e^- \rightarrow \gamma Z \rightarrow \gamma \mu^+ \mu^-$

Di-fermion production, with or without radiative return to the Z pole, is an integral part of the ILC physics case. In addition, the radiative return events offer an important opportunity to cross calibrate the energy scales of various subdetectors. As a detector benchmark, we chose here the example of calibrating the photon energy scale against the momentum scale of the tracker. Thereby, the momenta and angles of the muons as well as the polar and azimuthal angle of the photon serve as input, from which the energy of the photon and the amount of energy lost in beamstrahlung and collinear ISR are determined by requiring conservation of energy and p_y between initial and final state. It should be stressed that it is not necessary to apply a Z mass constraint, which would introduce an additional uncertainty due to the large natural width of the Z resonance. A full description of this and alternative methods can be found in [15].

Figure I-1.24 illustrates the power of this method by application to a non-perfectly calibrated photon reconstruction in the large detector model, both inclusively for all photons (Fig. I-1.24a) and in bins of the photon energy (Fig. I-1.24b). Since the $e^+e^- \rightarrow \mu^+\mu^-\gamma$ sample is dominated by radiative returns to the Z pole, the majority of photons has high energies close to 241 GeV.

The resolution of angular method, i.e. the width of the blue distribution in Fig. I-1.24a is shown for IDR-L and IDR-R in Fig. I-1.25a as a function of the photon energy. This translates into an absolute uncertainty on the photon energy scale calibration of about 10 MeV for high-energy photons, as shown in Fig. I-1.25b for the example of the large detector. [JL: what about small detector?]. The angular dependencies of the resolution of this method are shown in Fig. I-1.26. As a function of the polar angle, Fig. I-1.26a clearly shows the effect of the better momentum resolution of IDR-L for central high-momentum tracks, while in the two most forward bins, the small detector performs better due to its higher magnetic field. As a function of the azimuthal angle, the better resolution of the large detector is less pronounced, as can be seen in Fig. I-1.26b. The modulation of the resolution with ϕ is an effect of the beam crossing angle. This could be improved when exploiting all three momentum components in the balancing equations in a kinematic fit.

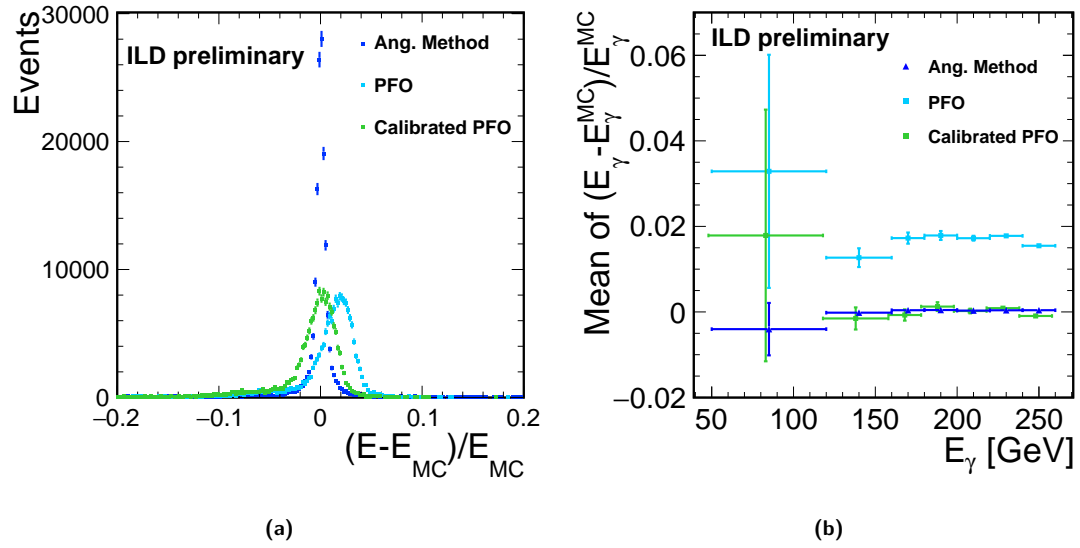


Figure I-1.24. Mean deviation of the photon energy from its true value when using non-perfectly calibrated PFO-level energies (cyan), when calculating the photon energy from the μ momenta and kinematic constraints (blue, “angular method”) and after calibrating the mean PFO-level w.r.t. the mean obtained from the μ momenta (green). (a) for all photons in the sample (b) in bins of the photon energy

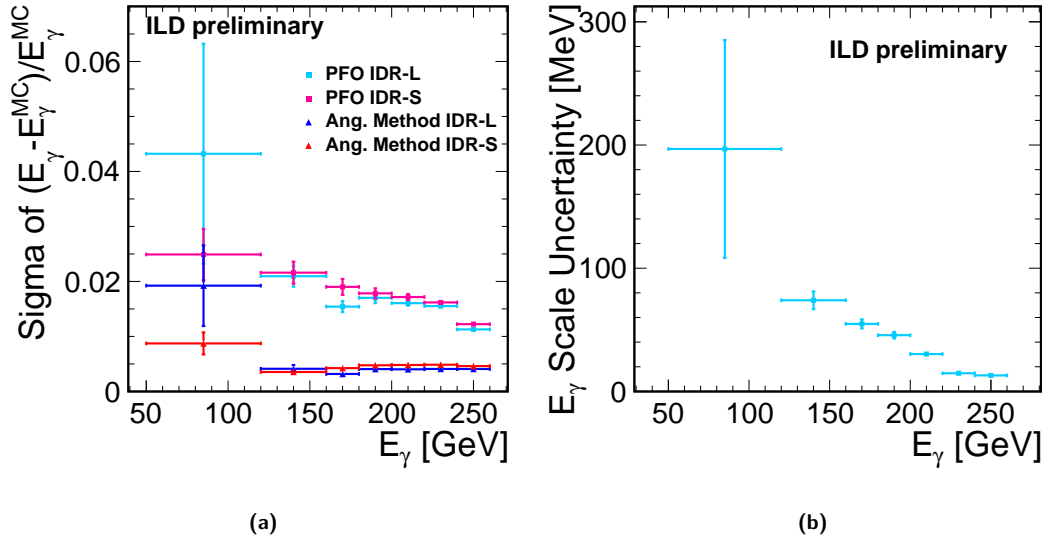


Figure I-1.25. Uncertainty on the photon energy scale calibration via the angular method as a function of the photon energy. (a) Relative uncertainty in % for IDR-L and IDR-S. (b) Absolute uncertainty in MeV (IDR-L only).

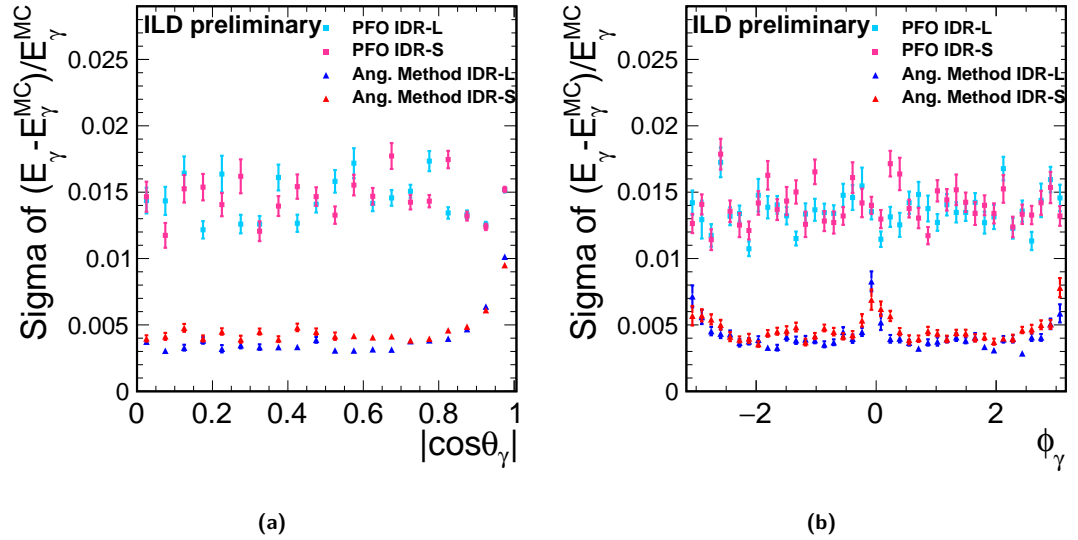


Figure I-1.26. Mean deviation of the photon energy from its true value when using non-perfectly calibrated PFO-level energies (cyan), when calculating the photon energy from the μ momenta and kinematic constraints (blue, “angular method”) and after calibrating the mean PFO-level w.r.t. the mean obtained from the μ momenta (green). (a) as a function of the polar angle (b) as a function of the azimuthal angle

1.3.8 A_{FB} and A_{LR} from $e^+e^- \rightarrow b\bar{b}$

The measurement of the left-right- and forward-backward asymmetries of b -quarks requires to distinguish the jet from the b -quark from the \bar{b} -jet. The two most important techniques for this are to reconstruct the charge of the secondary vertex, and to identify charged Kaons in the b -decay chain and exploit their charge. While the first method requires as complete reconstruction of all tracks from the secondary vertices as possible, the Kaon ID hinges upon a special feature of ILD, namely the measurement of the specific energy loss dE/dx in the TPC. In order to arrive at a reliable b -charge measurement, a consistent double-tag is required for each event, allowing for all four possible combinations of the two techniques. All details of the event reconstruction and selection can be found in [16].

Figure I-1.27a compares the acceptance of the b -jet reconstruction for the large and the small version of ILD. For $|\cos \theta_b| < 0.5$, corresponding to a large part of the endcap region, the acceptance of IDR-L is about 1% larger than for IDR-L. [JL: do we understand why? Loss of soft tracks due to higher B-field?] The purity of the four combinations of charge-ID (two methods times two jets) is shown in Fig. I-1.27b. While the charge-ID via vertex charge performs identically for both detectors, the Kaon-charge ID yields a higher purity for IDR-L due to the larger radius of the TPC, which improves the dE/dx resolution.

The final physics observable, namely the reconstructed $|\cos \theta_b|$ distribution, is shown for the example of 46 fb^{-1} of purely left-handed electron and purely right-handed positron data in Fig. I-1.28. The result for both detector models is compared to the parton-level distribution. [JL: what do we learn here? Any final precisions on A_{FB} and/or A_{LR} ?]

1.3.9 A_{FB} and A_{LR} from $t\bar{t} \rightarrow b\bar{b}q\ell\nu$

Building on the $e^+e^- \rightarrow b\bar{b}$ benchmark described in the previous section, the analogous study has also been performed for the case of $e^+e^- \rightarrow t\bar{t}$ [16]. So far, only the semi-leptonic channel has been analyzed, while the clean environment of a lepton collider in principle also allows to include the large statistics available in fully hadronic $t\bar{t}$ events. In order to prepare for the fully hadronic case, the vertexing and Kaon-ID based methods for charge identification have already been included

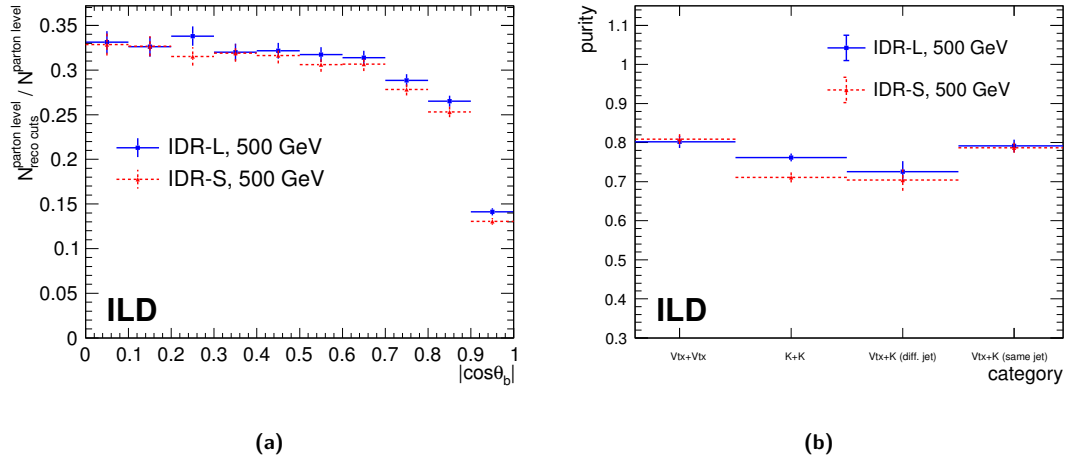


Figure I-1.27. (a) Acceptance of the $e^+e^- \rightarrow b\bar{b}$ analysis as a function of $\cos\theta_b$ of the b -quark for IDR-L and IDR-S. (b) Purity of the four different categories for charge tagging for IDR-L and IDR-S.

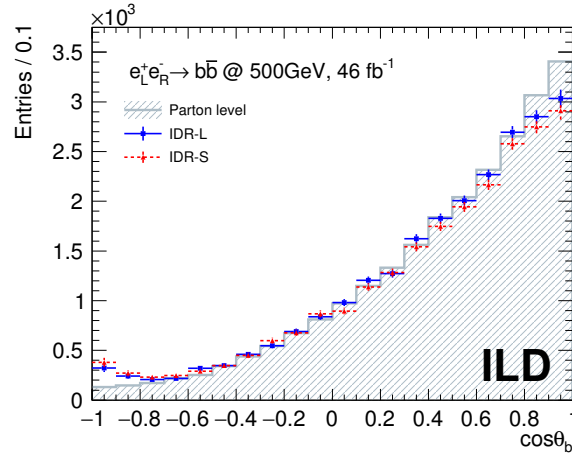


Figure I-1.28. Generator-level distribution of $\cos\theta_b$ and the corresponding reconstructed distributions for IDR-L and IDR-S. The distribution is shown for 46 fb^{-1} of pure $e_L^- e_R^+$ data.

in the analysis. The acceptances of the lepton-tag as well as of several double-tag combinations are compared for the large and small detector models in Fig. I-1.29. The single-tag based on the lepton charge (“ L_{cut} ”) is 100% efficient since the presence of a lepton is already required in the event selection. In fully hadronic $t\bar{t}$ events, only the double-tags without lepton information as shown in the first four bins, could be used, in analogy to the case of the $b\bar{b}$ analysis, c.f. Fig. I-1.27a. While the size of the detector has no direct influence on the semi-leptonic analysis, both the vertex and Kaon-ID based methods are more efficient in case of the large detector. [JL: Do we have any clue why there is a difference in the VTX tag?! The $b\bar{b}$ analysis does not show this...]

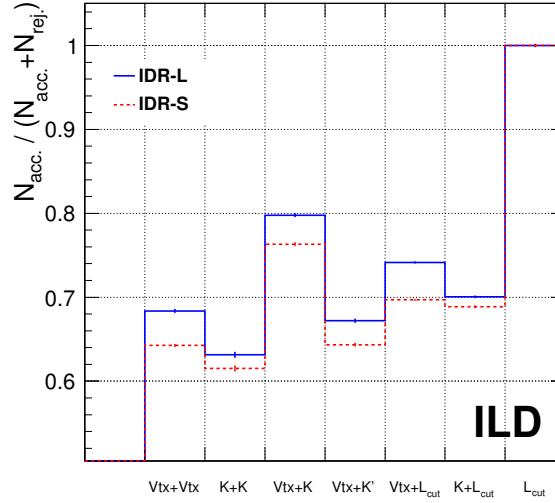


Figure I-1.29. Acceptance of various methods to identify the charge of the t/\bar{t} quarks. In the actual analysis, only the single-tag based on the lepton charge (“ L_{cut} ”) is used. The double-tag categories without lepton-tag are shown here as proxy for the fully hadronic channel. [JL: shouldn't we have a matching purity plot as well, like in Fig. I-1.27b?]

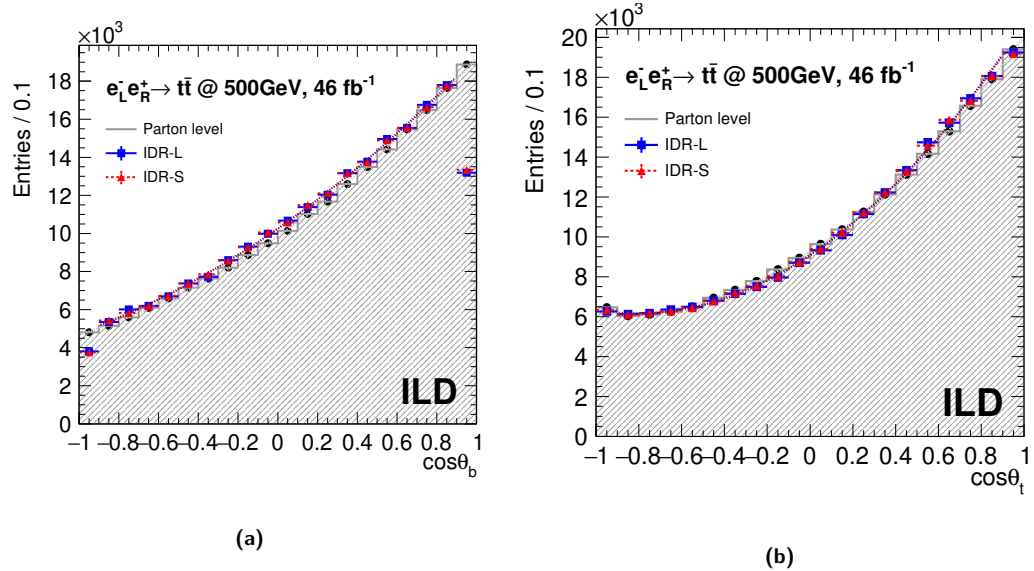


Figure I-1.30. Generator-level polar angle distributions and the corresponding reconstructed distributions for IDR-L and IDR-S. The distributions are shown for 46 fb^{-1} of pure $e_L^- e_R^+ \rightarrow t\bar{t}$ data. (a) Polar angle of the b -quark $\cos\theta_b$. (b) Polar angle of the t -quark $\cos\theta_t$.

The final physics observable, namely the reconstructed $|\cos\theta_t|$ distribution, is shown for the

example of 46 fb^{-1} of purely left-handed electron and purely right-handed positron data in Fig. I-1.30b, along with the corresponding distribution for the b -quark in Fig. I-1.30a. The results for both detector models are compared to the parton-level distribution. No difference is found here between the two detector models since the analysis is only based on the lepton-tag.

[JL:what do we learn here? Any final precisions on A_{FB} and/or A_{LR} ?]

1.3.10 Discovery Reach for extra Higgs Bosons in $e^+e^- \rightarrow Zh$

[material will be available on confluence by June 3, final presentation to ILD was on April 24]

Figure I-1.31. (a) (b)

1.3.11 Discovery Reach for and Characterisation of low ΔM Higgsinos

[no material available yet on confluence, final presentation to ILD tbd]

Figure I-1.32. (a) (b)

1.3.12 WIMP Discovery Reach and Characterisation in the Mono-Photon Channel

[preliminary material available on confluence, but suffering from BeamCal info being broken for IDR-L]

Figure I-1.33. (a) (b)

Bibliography

- [1] T. Barklow, J. Brau, K. Fujii, J. Gao, J. List, N. Walker, and K. Yokoya, “ILC Operating Scenarios” arXiv:1506.07830 [hep-ex].
- [2] P. Bambade *et al.*, “The International Linear Collider: A Global Project” arXiv:1903.01629 [hep-ex].
- [3] M. Kurata and R. Yonamine, “Higgs branching ratio study for new detector models as benchmark process in ILD”. <https://confluence.desy.de/display/ILD/ILD+notes>, 2019.
- [4] F. J. Mueller, *Development of a Triple GEM Readout Module for a Time Projection Chamber & Measurement Accuracies of Hadronic Higgs Branching Fractions in $\nu\nu H$ at a 350 GeV ILC*. PhD thesis, DESY, Hamburg, 2016. <http://bib-pubdb1.desy.de/search?cc=Publication+Database&of=hd&p=reportnumber:DESY-THESIS-2016-018>.
- [5] H. Ono, “Higgs branching ratio study for DBD detector benchmarking in ILD” in *Helmholtz Alliance Linear Collider Forum: Proceedings of the Workshops Hamburg, Munich, Hamburg 2010-2012, Germany*, pp. 203–223, DESY. DESY, Hamburg, 2013.
- [6] H. Ono and A. Miyamoto, “A study of measurement precision of the Higgs boson branching ratios at the International Linear Collider” *Eur. Phys. J.* **C73** (2013) no. 3, 2343, arXiv:1207.0300 [hep-ex].
- [7] J. Yan, S. Watanuki, K. Fujii, A. Ishikawa, D. Jeans, J. Strube, J. Tian, and H. Yamamoto, “Measurement of the Higgs boson mass and $e^+e^- \rightarrow ZH$ cross section using $Z \rightarrow \mu^+\mu^-$ and $Z \rightarrow e^+e^-$ at the ILC” *Phys. Rev.* **D94** (2016) no. 11, 113002, arXiv:1604.07524 [hep-ex].
- [8] J. Tian, “Higgs Mass Measurement at $\sqrt{s} = 500$ GeV as benchmark process in ILD”. <https://confluence.desy.de/display/ILD/ILD+notes>, 2019.
- [9] S. Kawada, “Branching ratio $H \rightarrow \mu^+\mu^-$ at $\sqrt{s} = 500$ GeV as benchmark process in ILD”. <https://confluence.desy.de/display/ILD/ILD+notes>, 2019.
- [10] Y. Kato, “ $H \rightarrow$ invisible at $\sqrt{s} = 500$ GeV as benchmark process in ILD”. <https://confluence.desy.de/display/ILD/ILD+notes>, 2019.
- [11] M. Boronat, J. Fuster, I. Garcia, E. Ros, and M. Vos, “A robust jet reconstruction algorithm for high-energy lepton colliders” *Phys. Lett.* **B750** (2015) 95–99, arXiv:1404.4294 [hep-ex].
- [12] D. Jeans and K. Yumino, “ τ polarisation in $e^+e^- \rightarrow \tau^+\tau^-$ at $\sqrt{s} = 500$ GeV as benchmark process in ILD”. <https://confluence.desy.de/display/ILD/ILD+notes>, 2019.
- [13] **ILD Concept Group**, T. Abe *et al.*, “The International Large Detector: Letter of Intent” arXiv:1006.3396 [hep-ex]. FERMILAB-LOI-2010-03, FERMILAB-PUB-09-682-E, DESY-2009-87, KEK-REPORT-2009-6.

- [14] J. Beyer, “Vector Boson Scattering at $\sqrt{s} = 1$ TeV as benchmark process in ILD”.
<https://confluence.desy.de/display/ILD/ILD+notes>, 2019.
- [15] T. Mizuno, “Calibration of the photon energy scale from $e^+e^- \rightarrow \gamma\mu^+\mu^-$ as benchmark process in ILD”. <https://confluence.desy.de/display/ILD/ILD+notes>, 2019.
- [16] A. Irles and Y. Okugawa, “ $e^+e^- \rightarrow b\bar{b}$ and $e^+e^- \rightarrow t\bar{t}$ as benchmark processes in ILD”.
<https://confluence.desy.de/display/ILD/ILD+notes>, 2019.